Activation of Lattice and Adatom Oxygen by Highly Stable Ceria-supported Cu Single Atoms

ACS Catalysis

pubs.acs.org/acscatalysis Research Article

Activation of Lattice and Adatom Oxygen by Highly Stable Ceria-Supported Cu Single Atoms

Carlos E. García-Vargas,[▽] Gregory Collinge,[▽] Dongmin Yun, Mal-Soon Lee,* Valery Muravev, Ya-Qiong Su, Xavier Isidro Pereira-Hernández, Dong Jiang, Vassiliki-Alexandra Glezakou, Emiel J. M. Hensen, Roger Rousseau, Abhaya K. Datye,* and Yong Wang*

Cite This: ACS Catal. 2022, 12, 13649−13662 Read Online

ACCESS | Metrics & More | Article Recommendations | Supporting Information

ABSTRACT: Requiring catalysts to be both active yet stable over long periods of time under variable reaction conditions including high and low temperatures is a daunting challenge due to the almost mutual exclusivity of these constraints. Using CO oxidation as a probe reaction, we demonstrate that thermally stable single-atom copper catalysts prepared by high-temperature synthesis (atom trapping) on ceria can achieve this feat by allowing modulation of the Cu charge state through facile charge transfer between the active site and the support. This provides the catalysts with an ability to activate either lattice or adatom oxygen atoms, accessing additional reaction channels as the catalyst environment changes. Such adaptability allows dynamic response of such catalysts, enabling them to remain active under variable reaction conditions. The inherent stability of the catalyst arises from the enhanced strength of the Cu−O interactions established by high-temperature synthesis and remains stable even as the Cu oxidation state varies, effectively halting sintering and deactivation. As we show here, one can circumvent the dilemma of designing catalysts that are simultaneously active and stable by matching the redox properties of the active site and support and establishing an environmental adaptability into the active sites.

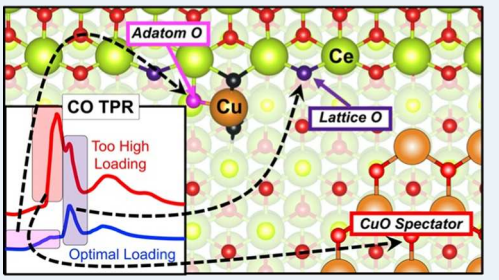

KEYWORDS: *single-atom catalysts, reducible oxide, charge shuttling, low-temperature CO oxidation, redox chemistry, vibrational density of states, ceria, copper*

INTRODUCTION

Maintaining catalyst durability over a wide range of operational temperatures and gas environments is among the most important challenge for exhaust emission abatement upon implementation of the most recent Environmental Protection Agency (EPA's) Tier 3 emission regulations.[1] Such regulations are pushing researchers and industry alike to develop durable catalytic technologies capable of removing up to 90% of automotive emissions (CO, hydrocarbons, NO_x) at temperatures as low as 150 °C while also remaining active and stable under frequent excursions to high temperatures (e.g., >750 °C). At the same time, it is necessary to make the best use of platinum group metals (PGMs) and/or developing alternative non-PGM catalytic materials.[2] The latter requirement is critical as emission control requires intensive use of PGMs, accounting for up to 50% of the global PGM demand.[3−5]

One of the most promising non-PGM catalysts for the removal of CO by low-temperature oxidation is Cu/CeO_2.[6] Studies on Cu/CeO_2 have used myriad synthesis methods, resulting in a wide variety of reported Cu structures. This has led to controversy over whether solid solution $Cu_xCe_{1-x}O_2$[7,8] or the interface of $CuO/Cu_xCe_{1-x}O_2$[9−12] are the active sites. For example, Elias et al.[7,13] were the first to propose that Cu^{3+}/Cu^{2+}−O−Ce redox centers (detected by X-ray absorption near-edge structure (XANES) during CO oxidation) in $Cu_xCe_{1-x}O_2$ solid solutions are the active sites where CO oxidation occurs. However, the authors neither clarified the role of the Cu−CO centers detected by diffuse reflectance infrared Fourier transform spectroscopy (DRIFTS) nor demonstrated their materials stability under thermal conditions.[13] On the other hand, Liu et al.[14] and Wang et al.[15] have recently reported that better low-temperature activity for CO oxidation can be achieved from $Cu_xCe_{1-x}O_2$ solid solutions if high-temperature calcinations are used (700−800 °C), proposing that the low-temperature active site is related to the interaction of segregated CuO_x clusters at the interphase of $Cu_xCe_{1-x}O_2$ solid solution. In contradiction to these findings, Yu et al.[16] made Cu/CeO_2 nanorods by thermal synthesis (calcination at 800 °C) and proposed that both CO and O_2 are activated exclusively at isolated Cu_1 sites but neglected the significant role of lattice oxygen from the reaction mechanism.

Received: August 12, 2022
Revised: October 5, 2022
Published: October 25, 2022

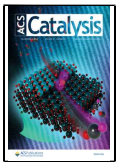

https://doi.org/10.1021/acscatal.2c04001
ACS Catal. 2022, 12, 13649−13662

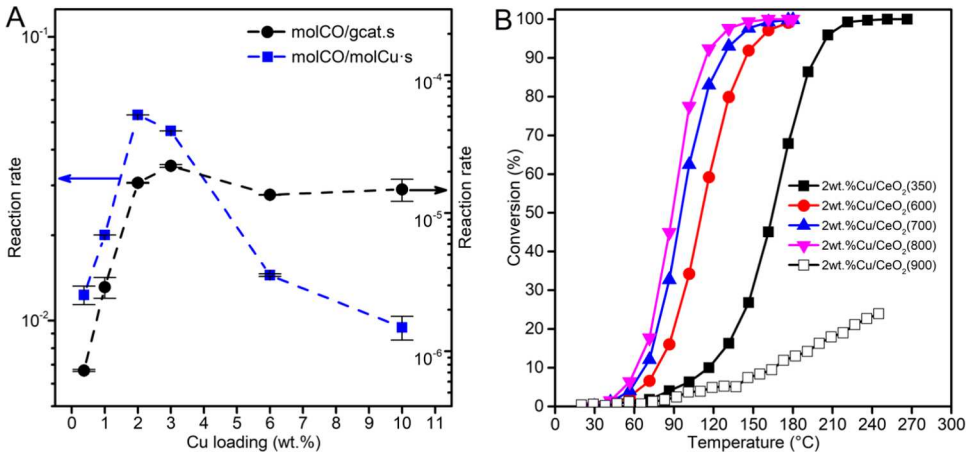

Figure 1. (A) CO oxidation reaction rate normalized by mol of Cu (blue squares) and gram of catalyst (black circles) for Cu_1/CeO_2 samples calcined at 800 °C, T = 70 °C, and X_{CO} < 10%; [CO] = 1%; [O_2] = 8%. (B) CO oxidation light-off curves for Cu_1/CeO_2 catalysts calcined at temperatures from 350 to 900 °C.

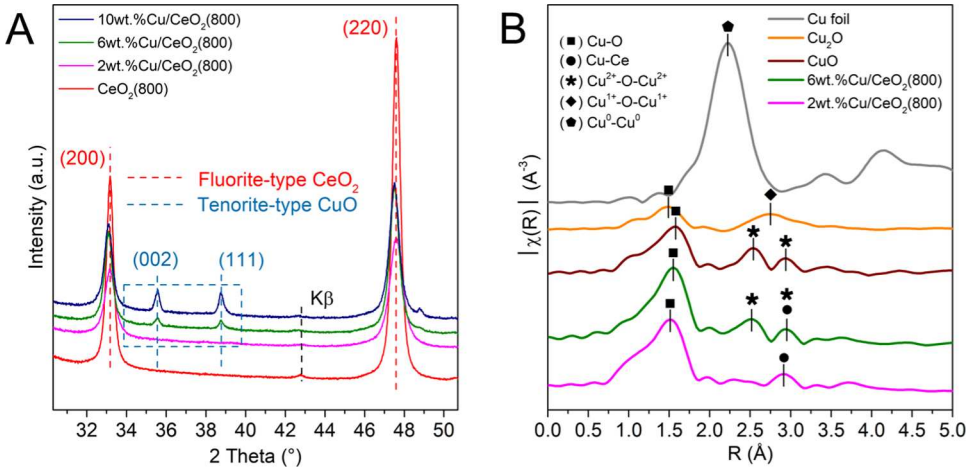

Figure 2. (A) XRD patterns of Cu/CeO_2 made by high-temperature calcination (800 °C) at different loadings along with a CeO_2 reference calcined at the same temperature (800 °C). (B) Extended X-ray absorption fine structure of Cu/CeO_2 catalysts with 0.37−6 wt % calcined at 800 °C and Cu references.

In the current study, we shine light on this debate by providing atomic-level understanding of why the highly desired coexistence of low-temperature reactivity and thermal durability properties, which are crucial for further development of emission abatement catalysts, are achieved only via high-temperature calcination (atom trapping).[17] Through a fully integrated experimental and theoretical approach, we explain that the rapid shuttling of electrons between atomically dispersed $(CuO)_1$ species and the support during CO oxidation create a dynamic charge center that allows semilocal control of the mobility of nearby oxygen species crucial for both low and high-temperature activity. This results in the intrinsic low-temperature activity of $(CuO)_1/CeO_2$, while its thermal stability is achieved through the anchoring of Cu atoms to $CeO_2(111)$ step sites, which are able to prevent sintering even under variable redox conditions or high temperatures.

RESULTS AND DISCUSSION

Catalytic Activity and Stability. The CO oxidation rate (molCO/molCu·s) over Cu/CeO_2 catalysts (Figure 1A) exhibits a pseudo-linear increase as a function of Cu loading up to a maximum at about ∼2 wt % Cu when calcined at 800 °C. Similarly, the best light-off performance was observed at the 2 wt % Cu content threshold (Figure S1), reaching a CO conversion of 100% at ∼150 °C. As the calcination temperature of the 2 wt % sample was increased from 350 to 800 °C, the CO oxidation light-off curves (Figure 1B) showed improved performance. Increasing the calcination temperature beyond 800 to 900 °C, however, resulted in a dramatic collapse of the light-off curve. To probe the catalyst's robustness under real vehicle exhaust conditions, the CO oxidation performance of the 2 wt % $Cu/CeO_2(800)$ catalyst was also evaluated using the Clean Diesel Combustion (CDC) protocol described by U.S. DRIVE.[18] The results were then compared with those of a reference 2 wt % Pt/CeO_2 catalyst subjected to the same protocol (Figure S2). After two consecutive light-off cycles, the 2 wt % $Cu/CeO_2(800)$ catalyst preserved its initial activity, while the 2 wt % Pt/CeO_2 reference catalyst, which already requires an initial reductive activation, lost catalytic activity due to the well-known reoxidation of Pt under lean conditions.[19] The initial light-off performance of the 2 wt % $Cu/CeO_2(800)$ catalyst after hydrothermal aging and after five consecutive CO oxidation cycles (Figures S3 and S4) was also preserved. Long-term

https://doi.org/10.1021/acscatal.2c04001
ACS Catal. 2022, 12, 13649−13662

stability was also observed (Figure S5). In all of the cases described, CO oxidation performance was remarkably resilient. In fact, the Cu/CeO_2(800) catalyst outperforms the standard Pt-based analogue [2 wt % Pt/CeO_2(800)] in terms of maintaining CO oxidation activity despite CO's equal competition with water for active sites.[20,21] Additionally, while poisoning with SO_2 (standard protocol) affected the CO oxidation light-off performance of the 2 wt % Cu/CeO_2(800) catalyst under CDC conditions (Figure S6A,B), the CO oxidation activity was fully recovered by oxidative thermal treatment. In the following sections, we provide a detailed understanding of the origin of this high CO oxidation activity and stability by elucidating the nature and structure of the active site within the Cu/CeO_2 catalyst whose intrinsic adaptability over a wide range of temperatures and environmental conditions is crucial for the development of next-generation emission control catalysts.

Structural Characterization. Surface area measurements (Table S1) corresponding to the samples shown in Figure 1A reveal that the presence of Cu positively correlates with higher surface area retention at calcination temperatures up to 800 °C with the surface area retention maximized (46 m^2/g) at 2 wt % Cu content as compared to pure ceria (23 m^2/g). For the high-loading 6 and 10 wt % Cu/CeO_2(800) samples, X-ray diffraction (XRD) diffractograms (Figure 2A) reveal aggregation of Cu to form the CuO phase, which is absent in the 2 wt % and lower Cu loading samples. The decrease in surface area observed in samples above 2 wt % Cu is a result of the presence of CuO on the CeO_2 surface. This CuO is less active than the atomically dispersed Cu, hence the rate per mole of Cu shows a plateau in CO oxidation reaction rates and light-off performance. Thus, in terms of the stabilization of CeO_2 surface area, a lower Cu content than 2 wt % is suboptimal, while in terms of activity, higher Cu content produces no further benefits. Cu surface density calculations (see details in the Methods section) indicate that 2 and 3 wt % have 4.20 and 7.15 Cu/nm^2, respectively. Lin et al. reported that a density threshold of 7.1 Cu^{2+}/nm^2, close to the Ce^{4+} surface density of CeO_2(111),[22] leads to the formation of CuO_x clusters.[23] Although CuO_x diffraction peaks were not observed in the 3 wt % Cu/CeO_2 sample (Figure S11), it is reasonable that at this loading and above, CuO_x clusters would form.

To better understand the local structure of the Cu species within the Cu/CeO_2 catalysts, extended X-ray absorption fine structure (EXAFS) analysis was carried out on Cu K-edge oscillations (Figure 2B). The collected EXAFS spectra for the 2 wt % Cu/CeO_2(800) catalyst exhibited only two features, which are commonly attributed to (■) first shell Cu−O and (●) second shell Cu−Ce bonds.[7,24] The exclusive presence of such coordination shells suggests that Cu is atomically dispersed.[8] On the other hand, the 6 wt % Cu/CeO_2 EXAFS spectrum displays three features: (■) first shell Cu−O bond, (★) a double peak (Cu^{2+}−O−Cu^{2+}) characteristic of bulk CuO presence,[8,24] and a convoluted (●) Cu−Ce bond. Therefore, the structure of the 6 wt % Cu sample can be interpreted as a mixture of atomically dispersed Cu sites and a segregated CuO phase, where the detection of the latter was corroborated by the described XRD measurements. No contributions of (◆) Cu^{1+}−O−Cu^{1+} or (⬟) Cu^0−Cu^0 coordination shells corresponding to Cu_2O and Cu^0 references[8] were detected.

High-angle annular dark-field scanning transmission electron microscope (HAADF/STEM) images of the 2 wt % Cu/CeO_2(800) catalyst allow us to visualize the lattice of CeO_2, exposing (111) crystal surfaces as well as notorious surface step defects (Figure S12A,B). Although atomically dispersed Cu cannot be directly observed due to poor Z-contrast between Cu and CeO_2,[25] neither segregated bulk CuO nor CuO_x clusters were detected by X-ray energy-dispersive spectroscopy (EDS) maps (Figure S12C,D). These oxidic Cu species have been reported in previous works with Cu loadings exceeding 2 wt %,[26,27] providing further evidence that Cu is atomically dispersed in the 2 wt % Cu/CeO_2(800) sample.

The charge nature of the atomically dispersed Cu species within the 2 wt % Cu/CeO_2(800) catalyst is revealed by Cu K-edge XANES spectra (Figure 3). Three main peaks at 8976, 8987, and 8998.4 eV are clearly observed in all of the Cu/CeO_2 catalysts. The lowest energy feature at 8976 eV (pre-edge feature) is characteristic of compounds containing Cu in a 2+ state.[13] The intermediate energy feature at 8987 eV is slightly blue-shifted (+2 eV) for the 2 wt % Cu/CeO_2(800) sample with respect to the CuO reference, which suggests that some fraction of the Cu species may also coexist in a slightly higher oxidation state than 2+, which was also reported recently.[13] A slight blue shift of the highest energy peak at 8998.4 eV in 2 wt % Cu/CeO_2(800) catalyst compared to 8997.2 eV for the CuO reference further suggests that the CuO phase is not present in the 2 wt % Cu/CeO_2(800) sample or in the lower Cu loadings, which agrees well with the previously described XRD and STEM analyses. The XANES spectrum of the 6 wt % Cu/CeO_2 sample (Figure 3) presented three main peaks at 8976, 8985, and 8997.7 eV. The lowest energy feature at 8976 eV, as already mentioned, is characteristic of a Cu 2+ oxidation state. The intermediate peak at 8985 eV coincides precisely with the corresponding feature of the CuO reference, which further demonstrates the presence of such a phase. The highest energy feature at 8997.7 eV is at an intermediate value between the same feature for the CuO reference (8997.2 eV) and the 2 wt % Cu/CeO_2(800) sample (8998.4 eV). This

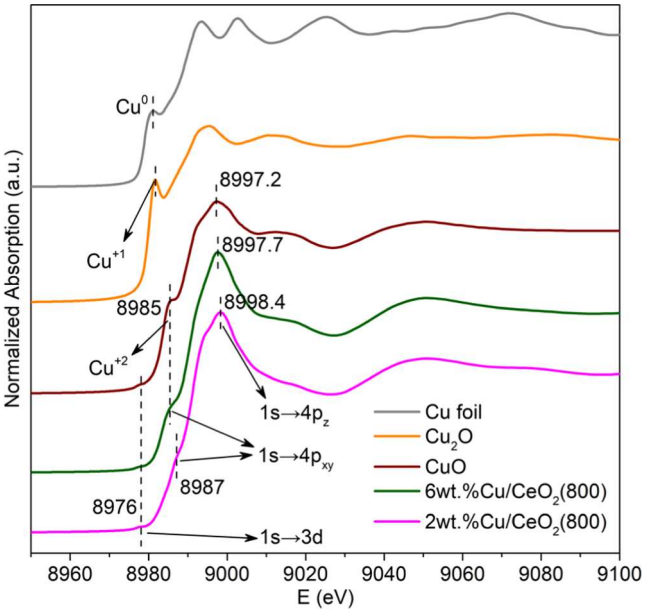

Figure 3. X-ray absorption near-edge structure of the Cu/CeO_2 catalyst with 2−6 wt % loadings made by calcination at 800 °C.

https://doi.org/10.1021/acscatal.2c04001
ACS Catal. 2022, 12, 13649−13662

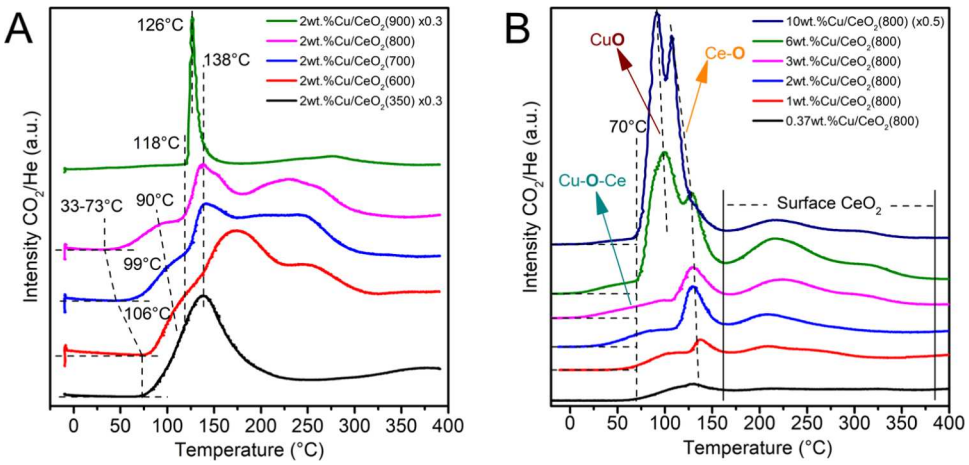

Figure 4. (A) CO-TPR for 2 wt % Cu/CeO_2 calcined at temperatures from 350 to 900 °C. (B) CO-TPR for Cu/CeO_2 with Cu content from 0.37 to 10 wt % calcined at 800 °C. The peak assigned to Ce−O on the 0.37 wt % Cu sample is shifted to lower temperatures as the Cu content increases up to 10 wt % Cu, likely due to a spillover effect.[28]

finding further supports the picture that the structural nature of Cu species within the 6 wt % Cu/CeO_2 sample can be understood as a coexistence of aggregated CuO and atomically dispersed Cu species, the latter being solely present in samples with lower loadings.

Activation of Lattice and Adatom Oxygen. The effects of calcination temperature and Cu content on the activation of lattice oxygen were studied by CO-temperature-programmed reaction (CO-TPR) experiments. When the calcination temperature used on the 2 wt % Cu/CeO_2 catalyst increases from 350 to 800 °C, a clear correlation is observed between better light-off performance (Figure 1B) and facile lattice oxygen activation at lower onset temperatures (Figure 4A). The onset temperatures of the light-off curves match well with those observed in the CO-TPR and decrease from ∼73 to ∼33 °C as the calcination temperature increases. A drastic loss in surface area to ∼5 m^2/g (Table S2) and the formation of a segregated CuO phase, as detected by XRD (Figure S13), explains the poor low-temperature oxygen activation of 2 wt % Cu/CeO_2 samples calcined at 900 °C.

The improvement of light-off performance with increased Cu content from 0.37 to 2 wt % (Figure S1) is correlated with lower onset temperatures and facile lattice oxygen activation observed in their respective CO-TPR profiles (Figure 4B). On samples with Cu content higher than 2−3 wt %, where CuO is detected by XRD and EXAFS, no further improvements to the onset temperatures are observed in their corresponding CO-TPR profiles. Based on these observations, we conclude that CuO does not improve activation of lattice oxygen at lower temperatures.

Examining the peak features from high to low temperature in the CO-TPR profiles, the reduction profiles of all Cu/CeO_2 samples at $T > 170$ °C (Figure 4B) are very similar to those of undoped CeO_2 samples that have been calcined at 800 °C (Figure S7B). Thus, such features are reasonably attributed to the reduction of the surface oxygen species of CeO_2 that have almost no interaction with Cu sites.[29] The peak at ∼131 °C is another common feature encountered in the reduction profiles of Cu/CeO_2 samples regardless of their Cu content and are reasonably attributed to the reduction of lattice oxygen from Ce−O species in closer proximity to Cu sites. The broad low-temperature reduction feature seen at $T < 70$ °C, which is present in all catalysts regardless of the Cu loading, is of great importance to understanding the activation of lattice oxygen. Polychronopoulou et al.[30] demonstrated by meticulous $^{18}O_2$ isotopic labeling and step-gas switch techniques that both adatom ("excess") and/or surface lattice oxygen are rapidly consumed under CO-only atmospheres to produce CO_2, and in the absence of O_2 to fill them, the resultant oxygen vacancies are slowly filled by subsurface lattice O. Being much slower than CO oxidation, this subsurface-to-surface lattice O diffusion process becomes rate limiting and leads to a broadening of the transient CO oxidation rate line traces. We believe that a similar subsurface diffusion phenomenon is responsible for the broadening of the low-temperature CO-TPR features discussed above for Figure 4B. Furthermore, when the amount of oxygen consumed at $T < 70$ °C was quantified from the CO-TPR and used to normalize the reaction rates of all 0.37−10 wt % $Cu/CeO_2(800)$ catalysts (as measured at $T = 70$ °C), a constant reaction stoichiometry close to 1:1 was revealed (Figure S8). Thus, we propose that the low-temperature reduction features seen in our CO-TPR results are reasonably assigned to the reduction of a single type of lattice or adatom oxygen species that is directly bound to the atomically dispersed Cu_1 sites.

We will briefly note that peak broadening can also be indicative of adspecies' coverage effects, but if repulsive interactions between adspecies were the primary reason for the broadening of the low-temperature reduction features seen in our CO-TPR profiles (Figure 4B), we would expect noticeable changes in their line shape[31−33] as the density of Cu_1 (and thus the density of Cu_1−CO and Cu_1−O species) increases from 0.37 to 2−3 wt %. The observed lower onset temperatures (Figure 4A,B) as Cu_1 density increases, on the other hand, are well correlated to the increased specific reaction rates observed (Figure 1A). Such an effect has been previously observed for Pd_1/CeO_2 single-atom catalysts and was explained by the cumulative enhancement of lattice oxygen reducibility due to long-range electrostatic effects that spatially overlap as Pd_1 density increases.[34] This is the only coverage effect we find to be of consequence.

Peaks at ∼91−100 °C are only seen in the CO-TPR profiles of 6−10 wt % Cu samples and can therefore be associated with reduction of the segregated CuO phase, whose presence was demonstrated by XRD and EXAFS. Note that while this (and the literature) shows CuO to be active in CO oxidation, our

https://doi.org/10.1021/acscatal.2c04001
ACS Catal. 2022, 12, 13649−13662

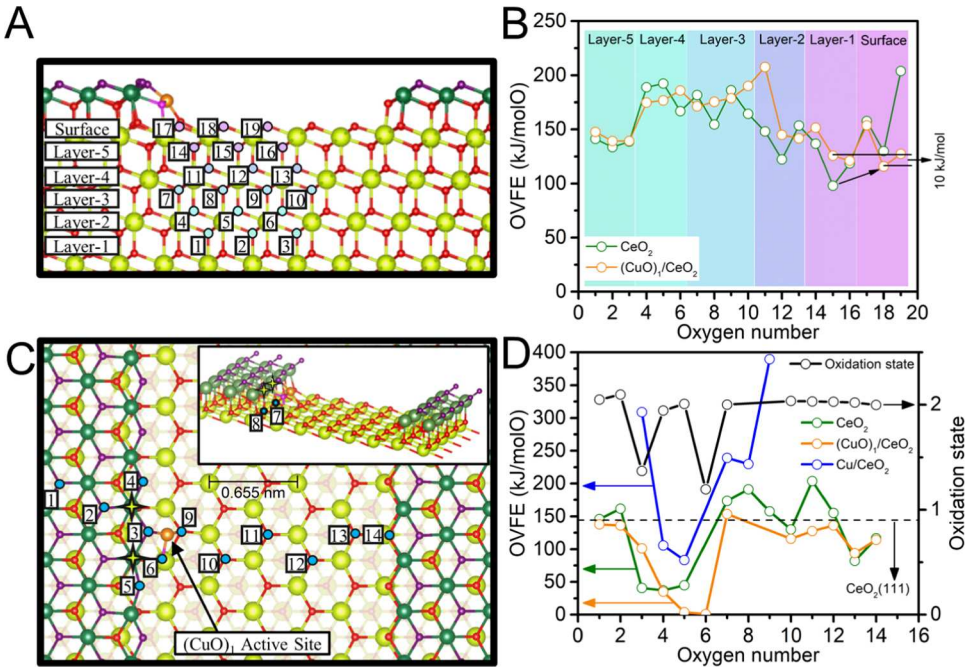

Figure 5. (A) Side view of the step-defected $Cu_1/CeO_2(111)$ surface model. Specific oxygen atoms have been numbered to aid discussion. Atom legend: dark green = upper terrace Ce, light green = lower terrace and subsurface Ce, purple = upper terrace O of CeO_2, red = lower terrace and subsurface O of CeO_2, orange = Cu, and magenta = O of $(CuO)_1$. (B) Oxygen vacancy formation energies (OVFE) of surface and subsurface oxygens labeled in panel (A) in the presence (orange) and absence (green) of the Cu atom. (C) Top-down view of step-defected $Cu_1/CeO_2(111)$ surface model (Inset: oblique view). Specific oxygen atoms have been numbered to aid discussion, and the Ce atoms directly above O atoms #7 and #8 have been indicated with yellow stars. (D) Oxygen vacancy formation energies (OVFEs) (orange, green, and blue lines) and resultant Cu oxidation states (black line) computed for oxygens labeled in panel (C). Orange: oxygen vacancy formation energies (OVFE) of labeled surface oxygens shown in panel (C). Note that OVFEs for O atoms #8 and #9 are missing due to instability: O#6 spontaneously refills their vacancies. Black: resulting Cu oxidation state after surface oxygen removal. Blue: OVFE of oxygens linking Cu to the support after initial removal of O#6. Green: OVFE for removal of surface oxygens labeled in panel (C) in the absence of the Cu atom.

analysis clearly shows that its specific activity and contribution to low-T light-off are limited compared to Cu single atoms and their activation of lattice O species. Therefore, we can conclude that at least two distinct types of lattice O species are involved in the reactivity, each formed by the introduction of Cu. These two species are both involved in low-temperature activity ($T \sim 35-130$ °C) and mid-temperature activity ($T \sim 130-170$ °C). Lastly, catalytic activity above 170 °C is indistinguishable from that of pure CeO_2.

Computational Model Validation. The results derived from density functional theory (DFT) calculations were obtained using a model (100)-step-defected $CeO_2(111)$ slab[35,36] where a $(CuO)_1$ single-atom center is trapped at the step defect (Figure 5A). The selection of such a model highlights the importance of the step defects for the stabilization of single metal atoms at high-temperature calcination conditions.[37,38] The proposed model was used to perform a fitting of the EXAFS spectra for the 2 wt % $Cu/CeO_2(800)$ and 6 wt % $Cu/CeO_2(800)$ catalyst samples. A reasonable fit of the first (Cu−O) and second (Cu−Ce) shells was obtained for the 2 wt % $Cu/CeO_2(800)$ sample, with calculated bond distances/coordination numbers (CNs) of 1.95 ± 0.01 Å/2.74 ± 0.25 and 3.26 ± 0.03 Å/2.98 ± 1.35, respectively (Figure S14A and Table S3). As an independent verification that accounts for finite-temperature effects, radial distribution functions ($g(r)$) were obtained from ab initio molecular dynamics (AIMD) trajectories (Figure S15) from which the ensemble-averaged Cu−O and Cu−Ce bond distances and CNs were extracted. The acquired values show excellent agreement with experimental EXAFS fits, producing an average Cu−O bond distance and CN of ∼1.90 Å (compared to 1.95 ± 0.01 Å) and ∼2.77 (compared to 2.74 ± 0.25), respectively (Figure S15A,C), and an average Cu−Ce bond distance of ∼3.35 Å (compared to 3.26 ± 0.03 Å) (Figure S15B,D). A broad distribution of the Cu−Ce $g(r)$ precluded an adequate coordination number assignment. For the 6 wt % $Cu/CeO_2(800)$ catalyst, the EXAFS fitting required a combination of both Cu_1 on steps of $CeO_2(111)$ and CuO paths for a successful fit, which yields first shell (Cu−O), second shell (Cu−Cu), and third shell (Cu−Ce) bond distances/coordination numbers of 1.94 ± 0.01 Å/3.99 ± 0.21, 2.88 ± 0.01 Å/1.20 ± 0.33, and 3.18 ± 0.01 Å/1.59 ± 0.39, respectively (Figure S14B and Table S4). The agreement between experimental and model-derived EXAFS confirms an accurate depiction of structural features around the active site of Cu/CeO_2 catalysts.

Further insights into the role of Cu and high-temperature calcination on the activation of lattice oxygen and thermal stability were revealed by calculations of oxygen vacancy formation energies (OVFE) as a function of their depth within the surface. These are labeled 1−19 in Figure 5A,B. For undoped $CeO_2(111)$ (green line in Figure 5B), lower OVFEs are obtained for O atoms in the first subsurface layer, implying that vacancies preferentially form subsurface. However, this trend is reversed by the presence of Cu (orange line in Figure 5B), which induces a small enthalpic driving force (∼10 kJ/mol/O) for oxygen vacancy diffusion to the surface. Further calculations reveal that strong Cu−O−Ce bonds (>300 kJ/

https://doi.org/10.1021/acscatal.2c04001
ACS Catal. 2022, 12, 13649−13662

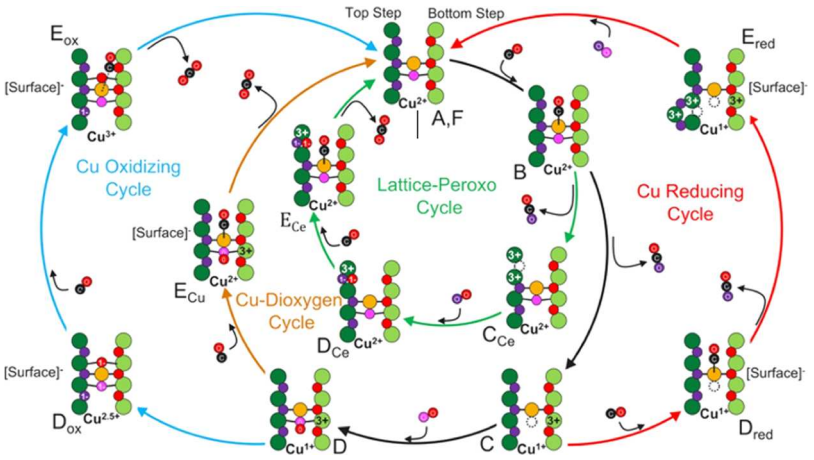

Figure 6. Four catalytic cycles identified in this work as potentially in operation during CO oxidation. Color coding is identical to that used in Figure 5C. The formal oxidation state of Cu is shown below each structure (to the nearest 0.5 |e⁻|). The oxidation state of Ce atoms are 4+ unless noted as "3+"; likewise, O atoms are 2− unless noted as "1−" or "0" (as in dioxygen). Reduction of surface atoms away from Cu is noted with "[surface]⁻".

mol/O) link the Cu^{2+} atom to the top (linked to oxygen #3 of Figure 5C) and bottom (linked to oxygen #9 of Figure 5C) of the step defect, which would easily prevent Cu diffusion and sintering if fully formed. Since roving oxygen vacancies can destabilize these bonds, pushing them to the surface and scavenging them during calcination in air is critical to stabilizing trapped Cu atoms at the step defect of $CeO_2(111)$. Since diffusion is accelerated with higher temperature, we can rationalize the observed dependence of catalyst stability and performance on the calcination temperature. The propensity of Cu atoms to form into a CuO phase at too-high Cu loadings regardless of the calcination temperature was found to result from a significantly favorable enthalpic driving force for $(CuO)_1$ agglomeration and oxidation (−79 kJ/mol/O, Figure S17). Once such CuO clusters are formed, the removal of its oxygen atoms becomes energetically much less favorable (+159 kJ/mol/O for the Cu−O−Cu species) compared to the single $(CuO)_1$ active center. This explains why at high Cu loadings the CuO phase is largely a spectator for low-temperature CO oxidation, becoming active only when temperatures are significantly elevated.

Catalytic Cycles and Free Energy Diagrams. Our model was further employed to investigate the molecular identity of the two types of active lattice oxygen that are responsible for low- and mid-temperature activity, as suggested by our experiments. For this, we used the computed OVFEs for the different types of oxygen present in the model (Figure 5C), which specifically exhibits three O species (lattice and adatom O) directly bound to Cu ("Cu−O−Ce species"), four−six lattice O species in close proximity to Cu ("proximal Ce−O species"), and many more lattice O species at progressively further distances from the active site.

The range of effect of the step-anchored Cu atom (orange line in Figure 5D) is striking: oxygen vacancy formation energy are notably impacted, with distances of at least 1.0 nm needed to recover the unmodified CeO_2 behavior (Figure 5D, after ∼O#12). Of all of these, three O species are far more removable than the others (labeled O# 4, 5, and 6 in Figure 5C,D): two proximal Ce−O species (O #4 and #5) and one Cu−O−Ce species (O#6, which is an O adatom). The proximal Ce−O species are both step edge lattice O, but only one (O#4) is accessible to a CO adsorbed to the Cu when the O adatom (O #6) is present. Thus, we can posit that the low-temperature active O species could correspond to either the Cu−O−Ce species (O#6), which exhibits nearly thermoneutral oxygen vacancy formation, or a proximal Ce−O species (O#4), which is removed at a cost of only ∼35 kJ/mol/O. We should note that while these values represent a low (or no) thermodynamic driving force for filling these vacancies with single O atoms, it is the driving force for O_2 adsorption into these vacancies that drives the reaction forward that is indeed exergonic as we will show shortly. We will therefore construct and test two separate CO oxidation cycles using both of these O species. However, to identify the mid-temperature active lattice O atom, we must consider the mobility of O atoms at higher temperatures after the lower temperature active O species has been reacted off in CO-TPR. To do this, we reassess the OVFEs of the lattice O again (blue series in Figure 5D) but this time after removing the most labile Cu−O−Ce species (i.e., O #6). This reveals that the proximal Ce−O species, while not as reactive as before, is still reactive enough (OVFE ∼ 83 kJ/mol/O) to be preferentially removed over unmodified CeO_2 (OVFE ∼ 145 kJ/mol/O). We therefore hypothesize that these proximal Ce−O species correspond to the observed mid-temperature active lattice O—though we must emphasize that both species are likely active under catalytic conditions. Another catalytic cycle will therefore be constructed based on the serial removal of these two species. Finally, since a Cu^{3+} active site has been invoked in the literature,[13] we also include an additional catalytic cycle that could conceivably form such a species.

The resulting network of nested catalytic cycles is shown in Figure 6 from which we derive four major pathways. The two cycles delineated with orange and green lines are built around CO oxidation by the Cu−O−Ce adatom species (colored pink) and proximal Ce−O species (colored purple), respectively. We term these the "Cu-dioxygen" and "lattice-peroxo" cycles after the location of their O species and the identity of the molecular O_2 that subsequently fills the vacancy. The cycle created by two sequential CO oxidation steps involving first the Cu−O−Ce and then the proximal Ce−O species results in the reduction of the Cu atom from 2+ to 1+ and is delineated with red lines and termed the "Cu-reducing" cycle accordingly. Finally, if one splits the adsorbed dioxygen

https://doi.org/10.1021/acscatal.2c04001
ACS Catal. 2022, 12, 13649−13662

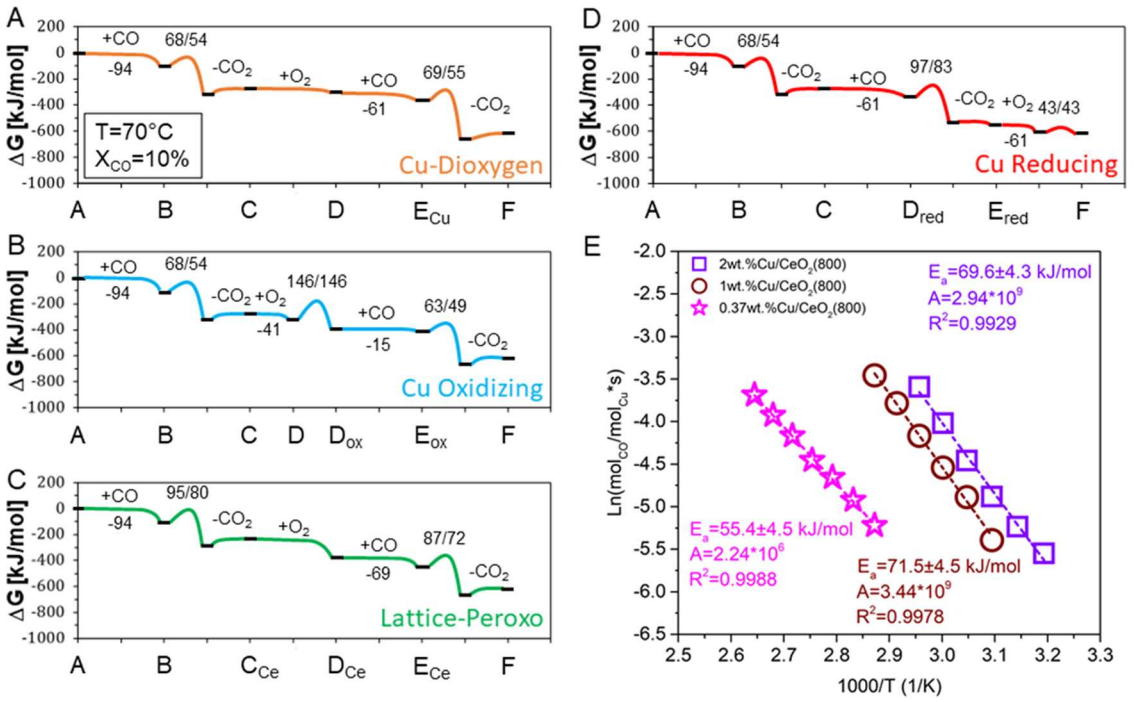

Figure 7. Computed (T = 70 °C and X_{CO} = 10%) free energy diagrams for (A) Cu-dioxygen cycle, (B) Cu oxidizing cycle, (C) lattice-peroxo cycle, and (D) Cu-reducing cycle. (E) Experimental Arrhenius plots of Cu_1/CeO_2 calcined at 800 °C with 2, 1, and 0.37 wt % Cu loading taken at X_{CO} < 10% (A = preexponential factors). The numbers split by a forward slash shown above each elementary reaction in panels (A–D) are the computed Gibbs free energy barrier (first number) and the intrinsic, 0 K energy barrier (second number) in units of kJ/mol.

across the Cu atom in the Cu-dioxygen cycle, Cu can be oxidized to 2.5+/3+. This forms our final cycle, the "Cu oxidizing" cycle, delineated with blue lines. Based on a Bader charge[39−43] calibration (Figure S18), formal charges (oxidation states) of all atoms in the system were computed at each step of each catalytic cycle and are shown in Figure 6. The results show that within each catalytic cycle, charge transfer between the support and metal center is common. Creating oxygen vacancies nearby the $(CuO)_1$ active center, filling them with O_2, and adsorbing CO all result in different distributions of charge scavenging/donation by Ce and Cu, with charge shuttling occurring rapidly between the two in response to each reaction step. Similar charge transfer effects have been reported by Polychronopoulou et al.[30] in their density of states studies of CeO_2 doped by several transition metals where doping with Cu resulted in the most significant charge transfer effects. In this context, it is interesting to highlight why two O species are missing from Figure 5C: O#8, a proximal Ce−O species lying beneath the $(CuO)_1$ active center along the negative [101] direction (we noted the location of the Ce atom directly above it with a yellow star in Figure 5C) and O#9, the lower step anchoring Cu−O−Ce species. This is because upon their removal, O#6 (the O adatom) spontaneously moves to refill their vacancies, reproducing a structure identical to the one after removing O#6. This process has no energetic barrier. This is highly demonstrative of the adatom's ability to dynamically respond to the redox state of the Cu_1 and CeO_2 supports, suggesting that a dynamic compensation behavior can be expected in response to the changing process and redox conditions during active catalysis, thus permitting reactive channels that would otherwise be disabled by such changes.

In Figure 7A–D, we determine adsorption and activation free energies for each elementary step in each aforementioned catalytic cycle. The computed activation free energy/intrinsic activation energy is presented for comparison against the experimentally measured apparent activation energy. The highest computed barriers (and, if ambiguous, their competitiveness against CO desorption) were used to identify likely rate determining steps (RDS) for each cycle, with the structure preceding each RDS making up the putative most abundant surface intermediate (MASI) of that cycle. In the molecular model used, the Cu concentration is near infinite dilution (≲0.16 wt % of entire model; ≲0.73 wt % of surface layer), making our computational results most comparable to the 0.37 wt % Cu sample. The Cu-dioxygen cycle (Figure 7A) exhibits the lowest overall barriers, and its RDS has an intrinsic activation energy of ∼54 kJ/mol, which is very consistent with the experimentally determined value of ∼55 kJ/mol for the 0.37 wt % Cu sample (Figure 7E). This suggests that low-temperature CO oxidation over Cu_1/CeO_2 proceeds primarily through the Cu-dioxygen cycle. Decreasing the distance between Cu single atoms by increasing loading to 1 and 2 wt % Cu induces a modest increase in the apparent activation barrier by ∼15 kJ/mol but a much larger increase in the preexponential factor by three orders of magnitude (Figure 7E). This observation is highly reminiscent of the surface density-dependent activity effect recently reported on Pd_1/CeO_2 by Kim et al.[34] This effect was tied directly to the redox properties of CeO_2, suggesting that we may be seeing the same phenomenon here. We remark this phenomenon as relevant to future research but beyond the scope of the current work. Nevertheless, the apparent activation barriers at 1 and 2 wt % Cu are still lower than the RDS barriers of the remaining catalytic cycles, lending credence to our assignment. For instance, splitting dioxygen (structure D in Figure 6) to enter the Cu-oxidizing cycle is kinetically inhibited (computed barrier of 146 kJ/mol) despite being exothermic (ΔG_{rxn} = −80

https://doi.org/10.1021/acscatal.2c04001
ACS Catal. 2022, 12, 13649−13662

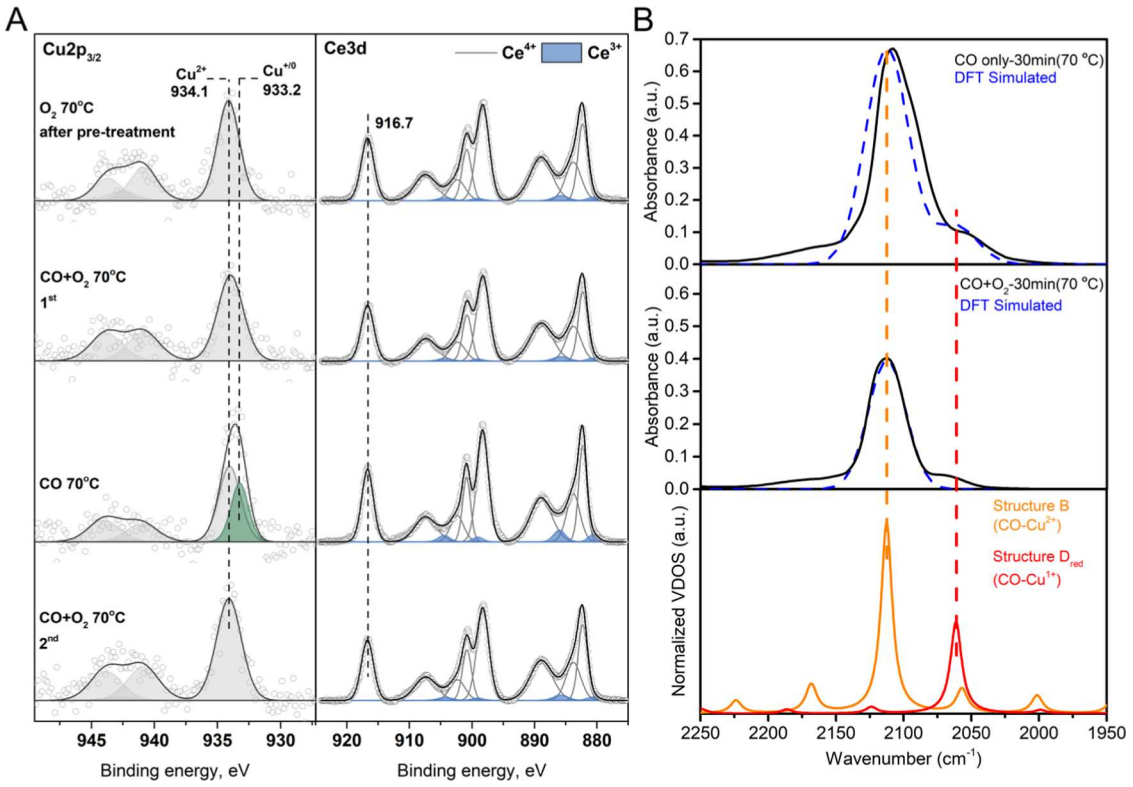

Figure 8. (A) Cu 2p and Ce 3d ambient-pressure X-ray photoelectron spectra (AP-XPS) of 2 wt % Cu_1/CeO_2 made by calcination at 800 °C. Experimental diffuse reflectance infrared Fourier transform spectroscopy (DRIFTS) spectra (black lines) of the Cu_1/CeO_2 catalyst vs. the corresponding density functional theory (DFT)-simulated DRIFTS (dashed blue lines), under (B) CO-only atmosphere (top) and a CO oxidizing atmosphere (middle). At the bottom of panel (B), normalized vibrational density of states (VDOS) peaks derived from AIMD of structure B (orange) and structure D_{red} (red) are shown.

kJ/mol). Any Cu^{3+} single-atom sites formed prior to the reaction will therefore reform only seldomly, making the Cu-oxidizing cycle likely inactive until higher temperatures are reached. The lattice-peroxo and Cu-reducing cycles are competitive with each other, each having a different RDS but a similar forward barrier (~95−97 kJ/mol). These two cycles are therefore most likely accessed in the mid-temperature range. We should note, however, that despite recent reports,[16] we see no evidence that an Eley−Rideal mechanism between molecular O_2 and bound CO is in play. Additionally, our measured reaction rate orders with respect to P_{CO} and P_{O_2} are 0.84 and 0.07, respectively (Figure S9). It is well acknowledged that a zero-order dependency on P_{O_2} strongly suggests that lattice oxygen is involved in the reaction mechanism, as it is encountered in our model and several previous works on Cu/CeO_2.[13,30]

Probing the Putatively Dominant Structures of Catalytic Cycles. We used near-ambient-pressure X-ray photoelectron spectroscopy (NAP-XPS) to probe and test the theoretically predicted MASI and its charge states during low-temperature CO oxidation. As seen in Figure 8A, under CO oxidizing conditions, only Cu^{2+} is detected—in agreement with our XANES results. For Ce, mostly Ce^{4+} is detected with a small amount of Ce^{3+}. If the Cu-dioxygen cycle is in operation during low-temperature CO oxidation as predicted, then structure B (exhibiting CO adsorbed to Cu^{2+}, "CO−Cu^{2+}") should be the MASI, but this structure displays no Ce^{3+}. However, the next-MASI along the Cu-dioxygen cycle is structure E_{Cu}, which still exhibits Cu^{2+} but with some Ce^{3+} present. A small representation of structure E_{Cu} amongst a MASI of otherwise structure B, CO−Cu^{2+}, is therefore consistent with the NAP-XPS results. We also consider what might happen if O_2 is cut off from the reaction (CO-only conditions). In this scenario, the MASI should still be primarily structure B, but the lowest barrier pathway forward without O_2 present is to progress to structure C and proceed specifically into the Cu-reducing cycle. Through theoretical calculations, Xie et al.[44] encountered that Cu−CO species tend to be redispersed and trapped by $CeO_2(111)$ step sites rather than sinter. The unchanged light-off curve of the 2 wt % $Cu/CeO_2(800)$ sample, before and after CO reduction at 200 °C (Figure S10), agrees with Xie's theoretical findings and our Cu-reducing cycle predictions. Nonetheless, it is noteworthy that such a mechanism of metal−carbonyl mobility seems to be metal dependent. While mobile Au−CO species tend to redisperse,[45,46] Pd−CO species tend to sinter.[47,48] Under low-temperature conditions, the reaction should largely stop at structure D_{red} (exhibiting CO adsorbed to Cu^{1+}, "CO−Cu^{1+}", as well as Ce^{3+}) due to a ~97 kJ/mol forward barrier. Thus, under CO-only conditions, one should expect a nonnegligible increase in Cu^{1+} and Ce^{3+} species according to the computational results. As can be seen in Figure 8A, this theoretical prediction is born out experimentally. Once O_2 is removed from the sample, NAP-XPS spectra exhibit a noticeable uptick in $Cu^{1+/0}$ and Ce^{3+} (Ce^{3+} fraction remains unchanged for bare CeO_2, see Figure S16 and Table S5), with the fraction of $Cu^{1+/0}$ present estimated at 0.15 (Table S5). This suggests that we have correctly identified the relevant

https://doi.org/10.1021/acscatal.2c04001
ACS Catal. 2022, 12, 13649−13662

catalytic cycles and their dominant MASIs for low-temperature CO oxidation.

To mitigate any remaining uncertainty and confirm the above assignments, we turn to vibrational spectroscopy. According to our DFT and NAP-XPS results, the MASIs in question here are predicted to contain ~100% structure B ($CO-Cu^{2+}$) when under CO oxidizing conditions and contain 85% structure B and 15% structure D_{red} ($CO-Cu^{1+}$) when under CO-only conditions (see Table S5 for detailed breakdown of these percentages). We should thus expect experimental infrared (IR) spectra collected under these two conditions to reproduce these predictions—both the composition and ratios. Simulated IR peaks constructed from DFT-derived vibrational frequencies of these MASI structures should thus match the experimental IR when combined in their predicted ratios. To ensure the most accurate computed values possible and account for the temperature used in the experiments, ab initio molecular dynamics (AIMD) simulations of each MASI structure were performed at 70 °C to extract anharmonic[49] and temperature-corrected CO stretch frequencies in the form of CO vibrational density of states (CO-VDOS) (see the Supporting Information for details). Diffuse reflectance infrared Fourier transform spectroscopy (DRIFTS) was then independently performed at 70 °C under CO oxidizing and CO-only conditions. The results are shown in Figure 8B. Under CO oxidizing conditions (prediction: ~100% $CO-Cu^{2+}$), DRIFTS detects one primary peak at 2112 cm^{-1}. Under CO-only conditions (prediction: ~85% $CO-Cu^{2+}$ and ~15% $CO-Cu^{1+}$), this peak red shifts slightly to ~2108 cm^{-1}, and a clear shoulder develops around the 2050 cm^{-1} region. The computed CO-VDOS for $CO-Cu^{2+}$ (structure B) is centered at 2112.5 cm^{-1}, in very good agreement with the primary DRIFTS peaks under both sets of conditions. The CO-VDOS for $CO-Cu^{1+}$ (structure D_{red}) is centered at 2061 cm^{-1}, which aligns very well with the shoulder developed under CO-only conditions. In the Cu_1/CeO_2 system, the 2050 cm^{-1} feature has never been assigned to any Cu−CO species, whereas the 2110 cm^{-1} species has been widely attributed to $CO-Cu^{1+}$, but such attribution has apparently been derived from imprecise extrapolation of Cu−CO assignments from Cu/SiO_2, Cu^0, and Cu/Al_2O_3 (Table S6). To construct our DFT-derived DRIFTS spectra for comparison with the experiment, we apply Gaussian functions to each primary CO VDOS peak weighted according to the fractions of Cu^{2+} (0.85) and Cu^{1+} (0.15) that are predicted to be present under CO-only conditions according to NAP-XPS (Table S5). The same process was applied to a single Gaussian centered around the primary CO VDOS peak at 2112.5 cm^{-1} to compare against the DRIFTS under CO oxidizing conditions. The *y*-scales were adjusted to align the peak maxima. This leaves no tunable parameters that could otherwise be used to perform a fitting. The resultant DFT-derived spectra are shown as dotted blue lines for CO-only and CO-oxidizing conditions in Figure 8B. The overall shape and placement of each DFT-simulated spectra are remarkably consistent with the experiment. In fact, a 6 cm^{-1} red shift, applied to the entire DFT-simulated spectrum in Figure 8B, is sufficient to produce a nearly perfect match (Figure S19) to the experimental spectra. Such a shift corresponds to an energy difference of ~0.07 kJ/mol, which is well within typically cited DFT errors (10−20 kJ/mol).

Based on the consistency between the theoretical predictions and experimental results, we conclude that the catalytic cycles and MASIs in operation during low-temperature CO oxidation over Cu_1/CeO_2 catalysts presented here have been correctly identified. This work thus demonstrates that flexible charge transfer between charge and support observed above contributes to the ability of the catalyst to adapt to the reaction environment and remain active, with strong anchoring to step defects providing its apparent stability.

CONCLUSIONS

We have shown here that low-temperature CO oxidation over Cu_1/CeO_2 proceeds via Cu single-atom active sites trapped at step defects, with Cu−O−Ce being the primary active oxygen species, both in the form of lattice oxygen and oxygen adatoms. We show that Cu cycles between 2+ and 1+ oxidation states during its primary catalytic cycle (the "Cu-dioxygen" cycle) with mostly $CO-Cu^{2+}$ making up the putative most abundant surface intermediate. It is especially interesting to note that as the temperature increases or partial pressure changes, other catalytic cycles can contribute to the reaction. A considerable debate in the literature concerning the active site of Cu_1/CeO_2 for CO oxidation can potentially be understood as a reflection of this concert of catalytic cycles producing a wide distribution of surface structures and potential charge states. Finally, we show that the remarkable robustness of this catalyst results from strong anchoring of Cu to step defects and its ability to adapt to changes in thermodynamic conditions while always manifesting a viable low-temperature route for CO oxidation.

METHODS

Experimental Details. *Catalyst Preparation.* Polyhedral CeO_2 support was prepared by thermal decomposition of cerium(III) nitrate hexahydrate ($Ce(NO)_3{\cdot}6H_2O$ 99% purity from Sigma-Aldrich) in air at 350 °C for 2 h.[50] The particle size was maintained between 0.149 and 0.125 mm with the use of 100 and 120 mesh number sieves. The Cu/CeO_2 catalysts of 0.37, 1, 2, 3, 6, and 10 wt % of Cu content were prepared by incipient wetness impregnation (IWI) of copper(II) nitrate trihydrate ($Cu(NO)_3{\cdot}6H_2O$ from Sigma-Aldrich) on the polyhedral ceria. After impregnation, the catalysts were dried in air at 150 °C for 1 h and cooled to room temperature for a second impregnation in the case of 6 and 10 wt % Cu content. Subsequently, we performed calcination at 350, 600, 700, and 800 °C (calcination at 800 °C is referred also as atom trapping[17]) for 10 h at a heating rate of 10 °C/min. A reference sample for the Clean Diesel Combustion test of 2 wt % Pt on CeO_2 calcined at 800 °C was prepared by the same IWI procedure. After calcination, the particle size was maintained between 0.149 and 0.125 mm with the use of 100 and 120 mesh number sieves. The samples are denoted as *x* wt %M/CeO_2(TTT) (M = metal used, *x* = wt % content, TTT = calcination temperature in °C).

Catalytic Activity. The CO oxidation reaction was conducted in an atmospheric pressure fixed-bed flow reactor system using the GC2060 gas chromatograph model by Shanghai Ruimin GC Instruments, Inc. The catalyst was loaded into a 4.0-mm-i.d. × 40.64-cm-long quartz tube packed in between inert quartz wool. The catalyst bed temperature was controlled with a PID temperature controller, and a thermocouple placed inside the quartz tube. The light-off curves were carried out using 20 mg of the catalyst and 500 mg of inert SiC, a heating rate of 2 or 3 °C/min and a GHSV of

https://doi.org/10.1021/acscatal.2c04001
ACS Catal. 2022, 12, 13649−13662

300,000 h^{-1}, 1% CO, 8% O_2, balanced helium. The reaction rates were calculated at a residence time approaching zero. The space velocity (inverse of residence time) was defined as ν/ω, where ν is the total flow rate in moles CO/s and ω is the moles Cu in the sample. Maintaining the X_{CO} less than 10%, the total flow rates were varied between 75 and 200 sccm/min, and the reaction rates were calculated using the X_{CO} previously determined with the GC measurements. Finally, the reaction rate at a residence time approaching zero was determined by a linear regression of the reaction rate versus the residence time plot. Activation energies were measured with 20 mg of the catalyst and 500 mg of inert SiC using 1% CO and 4% O_2 at 300,000 mL/g_{cat}·h while maintaining X_{co} less than 10%.

Characterization. Nitrogen Sorption Experiments. The nitrogen sorption experiments were conducted on a Micromeritics TriStar II 3020 physisorption analyzer at −196 °C using ultrahigh purity N_2. The specific surface areas of the catalysts were calculated based on the Brunauer−Emmett−Teller (BET) model. Catalysts were degassed at 300 °C for 1 h under vacuum before measurements were taken.

CO-TPR. The CO-TPR measurements were done with an Autochem 2920 from Micromeritics. The analysis of products was conducted with a Thermostar GSD 320 T Quadrupole Mass Spectrometer (QMS) from Pfeiffer Vaccum, equipped with a Secondary Electron Multiplier (SEM). Approximately 100 mg of the sample, a total flow rate of 100 sccm/min, and temperature ramps of 10 °C/min were used in all cases. An oxidative pretreatment was performed using 10% O_2/He while heating from room temperature to 400 °C and held for 60 min. Then, the temperature was decreased to −20 °C under ultrahigh purity (UHP) helium and maintained for 60 min until the QMS mass-to-charge ratios were stable. The temperature-programmed reduction was performed using 10% CO/He from −20 to 400 °C. The amount of CO_2 generated below 70 °C was calculated by calibrating the CO_2 signal using the QMS. Assuming that at low temperatures the CO-TPR follows the stoichiometry of CO + Cu−O* − Ce → CO_2 + Cu − [ ] − Ce, the amount of lattice oxygen participating in the low-temperature CO oxidation reaction was estimated directly from the measured CO_2 being produced. The proper selection of experimental conditions for temperature-programmed experiments was found to satisfy Monti[51] and Malet[52] criteria for optimal peak resolution. Transfer limitations were found absent by Gorte's[53−55] criteria evaluation. Additional details can be found in Section S7 (Tables S7 and S8).

X-ray Diffraction (XRD). XRD experiments were carried out with a Rigaku SmartLab using a Bragg−Brentano geometry and a DTex high-speed detector that allows for higher signal-to-noise ratio. The diffractograms were acquired using the Theta-2Theta scan axis in the range of 18−80°, a step of 0.01°, and a rate of 0.5°/min. X-ray diffractogram of 2 wt % Cu/CeO_2(900) was recorded by a Rigaku MiniFlex using similar parameters.

Calculation of Cu Density. Cu density calculations of 2 wt % Cu/CeO_2(800) and 3 wt % CuCeO_2(800) catalysts were carried out as indicated below

$$\frac{\text{Cu atoms}}{\text{nm}^2_{(CeO_2)}} = \frac{\frac{Cu_{wt\%}}{1-Cu_{wt\%}} \times \frac{1}{AW_{Cu}} \times Av_{\#}}{SA_{CeO_2} \times 10^{18}}$$

$Cu_{wt\ \%}$ = copper content in wt %; AW_{Cu} = atomic weight of Cu, which is 63.546 g/mol; $Av_{\#}$ = Avogadro's number; SA_{CeO_2} = experimental surface area of 2 wt % Cu/CeO_2 and 3 wt % Cu/CeO_2 catalysts calcined at 800 °C, obtained from the BET method (Table S1).

X-ray Absorption Spectroscopy (XAS). The XAS experimentation was performed at beamline 8-ID (ISS) of NSLS-II, Brookhaven National Laboratory. Cu-containing samples (100 mg for each) were pressed into a thin pellet with a diameter of 13 mm before installing in the sample holder. The XAS spectra of Cu K-edge were measured under a fluorescence model with a nickel foil filter. A Cu foil was measured simultaneously as a reference to calibrate the photon energy. Ten sweeps of data were collected for each sample and then merged for better signal quality. Standard compounds, Cu_2O and CuO, were diluted with BN (5 wt % in BN) before pellet making. Spectra of Cu_2O and CuO were collected under transmission mode. The data process and analysis follow the typical protocol,[56] including the energy calibration, merge, and Fourier transformation.

The collected X-ray absorption fine structure (XAFS) data were background-subtracted and normalized using the Athena software package. Extended X-ray absorption fine structure (EXAFS) fits were performed simultaneously in *R*-space on k^3, k^2, and k^1-weighted Cu K-edge spectra using Artemis. Scattering paths were calculated with FEFF8 using crystal structures of CuO and the density functional theory (DFT)-optimized CuO step model. The amplitude reduction factor S_0^2 was determined by fitting the Cu−Cu scattering paths, fixing the coordination number of a Cu foil reference sample to 12, and was found to be 0.876. The spectra were not phase-corrected.

Microscopy Imaging. The samples were sieved using a 100-mesh number grid. Subsequently, a small amount of powder was thoroughly dissolved in ethanol and further deposited on a 200 mesh Lacey carbon Au grid, where ethanol was fully evaporated before imaging. Images were acquired using a Thermo Fisher Scientific Themis Z 30-300 STEM operating at 300 kV. High-resolution imaging was performed in STEM mode using a convergence angle of 25 mrad. The images were collected using high-angle annular dark-field detector in an annular range of 51−200 mrad. X-ray energy-dispersive spectroscopy (EDS) was performed with a Super-X G2 detector. The acquisitions were made with probe currents in the range of 45−50 pA for the analyzed sample. Dwell times of 20 μs were used for high-resolution maps that were obtained with multiframe (300 frames) drift-corrected acquisition. EDS data processing was performed with Velox software from Thermo Fisher Scientific.

Near-Ambient-Pressure X-ray Photoelectron Spectroscopy (NAP-XPS). The surface chemistry of Cu/CeO_2 catalysts was characterized in a laboratory-based SPECS NAP-XPS system. Cell-in-chamber design of the spectrometer allows in situ XPS measurements at pressures of up to 2 mbar (controlled via back-pressure regulator installed at the outlet of the cell) using high-purity gases fed into the NAP-cell via calibrated mass-flow controllers. Powder catalysts were mixed with the inert carbon diluent and pelletized into self-supporting pellets to provide sufficient conductivity for obtaining high-quality XPS spectra. Prior to the reaction, the catalysts were pretreated in 2 mbar of pure O_2 (2 mL/min) at 300 °C to desorb water and loosely bound carbonate species. A reaction mixture of 0.5 mL/min of CO and 2 mL/min of O_2 was used to mimic oxygen-rich conditions of catalytic tests in the plug flow reactor. A standard residual gas analyzer placed in the

https://doi.org/10.1021/acscatal.2c04001
ACS Catal. 2022, 12, 13649−13662

second differential pumping stage allowed following the catalytic activity during XPS measurements. Further technical details about the NAP-XPS system can be found in the literature.[57] Spectra were obtained using monochromatic Al Kα irradiation (1486.6 eV) of an Al source operating at 50 W. The total acquisition time of the survey and regions of interest took around 90−120 min. A pass energy of 40 eV with a step size of 0.1 eV and a dwell time of 0.5 s was typically used for acquiring the core-line spectra. For the sake of acquisition time, only Cu $2p_{3/2}$ component of Cu 2p core line was collected. The Cu $2p_{3/2}$, Cu LMM, and Ce 3d regions were energy-corrected according to the U‴ component of the Ce 3d core line with a characteristic binding energy of 916.7 eV.[58−60] The peak position of this component is independent of the Ce^{3+} to Ce^{4+} ratio (as long as Ce^{4+} is present), which makes it possible to calibrate the spectra throughout the experiment. Atomic ratios were estimated following the standard procedure, involving a Shirley background subtraction and raw area normalization using relative sensitivity factors. Spectral lines were fitted using a symmetric pseudo-Voigt function denoted by a GL line shape in the Casa XPS software. The Ce 3d line was fitted according to a model described elsewhere.[59,61] All of the spectra are presented without normalization of the areas. The Cu/Ce atomic ratios as a function of temperature and gas phase were estimated to follow possible sintering/segregation of Cu.

Diffuse Reflectance Infrared Fourier Transform Spectroscopy (DRIFTS). DRIFTS spectra were acquired with a Tensor 27 from Bruker, coupled with a Praying Mantis Diffuse Reflection Accessory from Harrick. Approximately 50−60 mg of the sample was used for the experiment. An initial pretreatment was done with 10% O_2/He at 300 °C for 30 min to remove moisture and loosely bound carbonate species. Afterward, the sample was cooled to 70 °C and a background was taken after flowing 50 mL/min of He for 30 min. Spectra taken during CO oxidation were collected for ∼30 min, starting immediately after the sample was exposed to 6 mL/min of 10% CO/He (1% CO), 30 mL/min of He, and 24 mL/min of 10% O_2/He (4% O_2). After CO oxidation, spectra were taken when the sample was exposed to 6 mL/min 10% CO/He (1% CO) and 54 mL/min of He for ∼30 min. After exposing the sample to CO-only, CO oxidation spectra were taken once again for 30 min at 1% CO and 4% O_2.

Further experimental details are provided in Section S4.

Computational Methods. Our proposed model of the Cu/CeO_2 single-atom active site exhibits a long CeO_2(111) terrace into which a step defect has been created by cleaving the top row along the [110] direction, exposing two different step edges. The leftmost top-step edge exposes a (100)-like facet and is the dominant step edge of CeO_2 according to Freund and co-workers,[35,36] and so a $(CuO)_1$ single active center is placed there. The model is shown in Figures 5A and S20. The opposing step edge is (111)-like and is an unavoidable artifact of cleaving CeO_2 along a nonsymmetry plane of its fluorite structure. The model is made up of four full CeO_2 layers (representing the bulk and lower terrace) and one (half-cleaved) layer of CeO_2 atop this (representing the upper terrace), and thus, in total, the simulation supercell is comprised of 225 CeO_2 formula units or 675 atoms not including the added $(CuO)_1$ active site or molecular adspecies. Periodic boundary conditions are employed throughout.

Computed energetics were derived from DFT calculations using the CP2K quantum chemical package.[62] Geodecker−Teter−Hutter (GTH) pseudopotentials were used to describe the core region of each atom,[63] while valence electrons were described in a Gaussian plane wave hybrid basis set scheme.[64] To adequately describe the f-orbitals in Ce, a recently published, more accurate Ce basis set and GTH pseudopotential were used[65,66] along with its corresponding (Mullikan charge based) optimized Hubbard U parameter.[67] Free energies of gas-phase molecules were evaluated using standard statistical mechanical methods,[66] while those of the adspecies were approximated using Campbell and Seller's measured entropy correlations.[68] AIMD simulations were performed in the canonical NVT ensemble using a Nosé−Hoover thermostat[69,70] from which fully anharmonic CO vibrational density of states (VDOS)[71] were derived to compare against IR experiments. Model electrostatics (Figure S21) and further computational details can be found in Section S3.

■ ASSOCIATED CONTENT

Supporting Information

The Supporting Information is available free of charge at https://pubs.acs.org/doi/10.1021/acscatal.2c04001.

Appendix S1_Structural Data-$CuCeO_2$ (PDF)

Cu wt % influence on CO oxidation light-off curves; activity of 2 wt % Cu/CeO_2(800) under clean diesel combustion (CDC) and effect of SO_2 poisoning/regeneration; TOS, thermal, cyclic, reductive, and hydrothermal stabilities of 2 wt % Cu/CeO_2(800) for CO oxidation; CO-TPR profiles and analysis of transfer effects; CO oxidation reaction rates and dependencies to P_{co} and P_{O_2} partial orders; X-ray diffraction of 3 wt % Cu/CeO_2(800) and 2 wt % Cu/CeO_2(900); STEM/EDS of 2 wt % Cu/CeO_2(800); XAS data and fitting of 2 wt % Cu/CeO_2(800) and 6 wt % Cu/CeO_2(800); AP-XPS spectra of bare CeO_2 and quantification of $Cu^{+/0}$ and Ce^{3+} fractions on 2 wt % Cu/CeO_2(800); computational agglomeration of $(CuO)_1$; determination of Cu and Ce formal charges in the model; DFT-simulated IR and table of literature reported Cu−O IR assignments on several Cu-containing catalytic systems; description of computational model and methods; and surface area of Cu/CeO_2 catalysts (PDF)

■ AUTHOR INFORMATION

Corresponding Authors

Mal-Soon Lee − *Institute for Integrated Catalysis, Pacific Northwest National Laboratory, Richland, Washington 99354, United States;* orcid.org/0000-0001-6851-177X; Email: malsoon.lee@pnnl.gov

Abhaya K. Datye − *Department of Chemical and Biological Engineering and Center for Micro-engineered Materials, University of New Mexico, Albuquerque, New Mexico 87131, United States;* orcid.org/0000-0002-7126-8659; Email: datye@unm.edu

Yong Wang − *The Gene and Linda Voiland School of Chemical Engineering and Bioengineering, Washington State University, Pullman, Washington 99164, United States; Institute for Integrated Catalysis, Pacific Northwest National Laboratory, Richland, Washington 99354, United States;* orcid.org/0000-0002-8460-7410; Email: yong.wang@pnnl.gov

https://doi.org/10.1021/acscatal.2c04001
ACS Catal. 2022, 12, 13649−13662

Authors

Carlos E. García-Vargas − *The Gene and Linda Voiland School of Chemical Engineering and Bioengineering, Washington State University, Pullman, Washington 99164, United States; Environmental Molecular Sciences Laboratory, Richland, Washington 99354, United States;* orcid.org/0000-0001-7486-9604

Gregory Collinge − *Institute for Integrated Catalysis, Pacific Northwest National Laboratory, Richland, Washington 99354, United States;* orcid.org/0000-0001-8345-6254

Dongmin Yun − *The Gene and Linda Voiland School of Chemical Engineering and Bioengineering, Washington State University, Pullman, Washington 99164, United States*

Valery Muravev − *Laboratory of Inorganic Materials and Catalysis, Department of Chemical Engineering and Chemistry, Eindhoven University of Technology, 5600 MB Eindhoven, The Netherlands;* orcid.org/0000-0002-1357-1086

Ya-Qiong Su − *Laboratory of Inorganic Materials and Catalysis, Department of Chemical Engineering and Chemistry, Eindhoven University of Technology, 5600 MB Eindhoven, The Netherlands*

Xavier Isidro Pereira-Hernández − *The Gene and Linda Voiland School of Chemical Engineering and Bioengineering, Washington State University, Pullman, Washington 99164, United States; Institute for Integrated Catalysis, Pacific Northwest National Laboratory, Richland, Washington 99354, United States;* orcid.org/0000-0002-7020-0011

Dong Jiang − *The Gene and Linda Voiland School of Chemical Engineering and Bioengineering, Washington State University, Pullman, Washington 99164, United States;* orcid.org/0000-0003-0444-7865

Vassiliki-Alexandra Glezakou − *Institute for Integrated Catalysis, Pacific Northwest National Laboratory, Richland, Washington 99354, United States;* Present Address: Chemical Science Division, Oak Ridge National Laboratory, Oak Ridge, Tennessee 37830, United States; orcid.org/0000-0001-6028-7021

Emiel J. M. Hensen − *Laboratory of Inorganic Materials and Catalysis, Department of Chemical Engineering and Chemistry, Eindhoven University of Technology, 5600 MB Eindhoven, The Netherlands;* orcid.org/0000-0002-9754-2417

Roger Rousseau − *Institute for Integrated Catalysis, Pacific Northwest National Laboratory, Richland, Washington 99354, United States;* Present Address: Chemical Science Division, Oak Ridge National Laboratory, Oak Ridge, Tennessee 37830, United States; orcid.org/0000-0003-1947-0478

Complete contact information is available at: https://pubs.acs.org/10.1021/acscatal.2c04001

Author Contributions

[▽]C.E.G.-V. and G.C. contributed equally. Experiments were performed by C.E.G.-V., D.Y., V.M., Y.-Q.S., X.I.P.-H., and D.J. with computations performed by G.C. and M.-S.L. All authors collaborated on the design of the research and preparation of the manuscript.

Notes

The authors declare no competing financial interest.

■ ACKNOWLEDGMENTS

The experimental effort (catalyst synthesis and characterization via TEM and DRIFTS, etc.) was supported by the DOE/BES Catalysis Science Program, Grant DE-FG02-05ER15712. Theory effort was supported by the US Department of Energy (US-DOE) Basic Energy Sciences, Chemical Sciences, Geosciences and Biosciences Division, Catalysis Program (FWP 47319). C.E.G.-V., X.I.P.-H., and D.J. thank the funding support from US-DOE Energy Efficiency and Renewable Energy Vehicle Technology Office. C.E.G.-V. and X.I.P.-H thank Fulbright Colombia and *Colciencias* for the financial support provided to pursue their Ph.D. The computer resources were provided by the PNNL Research Computing facility and the National Energy Research Center (NERSC) located at LBNL. The authors thank Libor Kovarik for the help in the acquisition of the STEM/EDS images at EMSL facilities.

■ REFERENCES

(1) US Environmental Protection Agency. Federal and California Light-Duty Vehicle Emissions Standards for Air Pollutants. https://nepis.epa.gov/Exe/ZyPDF.cgi?Dockey=P100XCIV.pdf.

(2) U.S. D.R.I.V.E. Partnership. *Advanced Combustion and Emission Control Roadmap (2018)*; 2018.

(3) Twigg, M. V. Catalytic Control of Emissions from Cars. *Catal. Today* **2011**, *163*, 33−41.

(4) Hagelüken, C.; Buchert, M.; Stahl, H. Substantial Outflows of Platinum Group Metals Identified: Spent Autocatalysts Are Systematically Withdrawn from the European Market. *World Metall.–Erzmet.* **2003**, *56*, 529−540.

(5) Granger, P.; Parvulescu, V. I. Catalytic NOx Abatement Systems for Mobile Sources: From Three-Way to Lean Burn after-Treatment Technologies. *Chem. Rev.* **2011**, *111*, 3155−3207.

(6) Liu, W.; Flytzani-Stephanopoulos, M. Transition Metal-Promoted Oxidation Catalysis by Fluorite Oxides: A Study of CO Oxidation over Cu/CeO_2. *Chem. Eng. J. Biochem. Eng. J.* **1996**, *64*, 283−294.

(7) Elias, J. S.; Artrith, N.; Bugnet, M.; Giordano, L.; Botton, G. A.; Kolpak, A. M.; Shao-Horn, Y. Elucidating the Nature of the Active Phase in Copper/Ceria Catalysts for CO Oxidation. *ACS Catal.* **2016**, *6*, 1675−1679.

(8) Yoshida, H.; Okabe, Y.; Misumi, S.; Oyama, H.; Tokusada, K.; Hinokuma, S.; Machida, M. Structures and Catalytic Properties of Cr−Cu Embedded CeO_2 Surfaces with Different Cr/Cu Ratios. *J. Phys. Chem. C* **2016**, *120*, 26852−26863.

(9) Jia, A.-P.; Hu, G.-S.; Meng, L.; Xie, Y.-L.; Lu, J.-Q.; Luo, M.-F. CO Oxidation over CuO/$Ce_{1-x}Cu_xO_{2-d}$ and $Ce_{1-x}Cu_xO_{2-d}$ Catalysts: Synergetic Effects and Kinetic Study. *J. Catal.* **2012**, *289*, 199−209.

(10) Liu, W.; Flytzani-Stephanopoulos, M. Total Oxidation of Carbon-Monoxide and Methane over Transition Metal Fluorite Oxide Composite Catalysts: II. Catalyst Characterization and Reaction-Kinetics. *J. Catal.* **1995**, *153*, 317−332.

(11) Yao, S.; Mudiyanselage, K.; Xu, W.; Johnston-Peck, A. C.; Hanson, J. C.; Wu, T.; Stacchiola, D.; Rodriguez, J.; Zhao, H.; Beyer, K. A.; Chapman, K. W.; Chupas, P. J.; Martínez-Arias, A.; Si, R.; Bolin, T. B.; Liu, W.; Senanayake, S. D. Unraveling the Dynamic Nature of a CuO/CeO_2 Catalyst for CO Oxidation in Operando: A Combined Study of XANES (Fluorescence) and DRIFTS. *ACS Catal.* **2014**, *4*, 1650−1661.

(12) Zhou, Y.; Chen, A.; Ning, J.; Shen, W. Electronic and Geometric Structure of the Copper-Ceria Interface on Cu/CeO_2 Catalysts. *Chin. J. Catal.* **2020**, *41*, 928−937.

(13) Elias, J. S.; Stoerzinger, K. A.; Hong, W. T.; Risch, M.; Giordano, L.; Mansour, A. N.; Shao-Horn, Y. In Situ Spectroscopy and Mechanistic Insights into CO Oxidation on Transition-Metal-Substituted Ceria Nanoparticles. *ACS Catal.* **2017**, *7*, 6843−6857.

(14) Wang, B.; Zhang, H.; Xu, W.; Li, X.; Wang, W.; Zhang, L.; Li, Y.; Peng, Z.; Yang, F.; Liu, Z. Nature of Active Sites on Cu-CeO_2

Catalysts Activated by High-Temperature Thermal Aging. *ACS Catal.* **2020**, *10*, 12385−12392.
(15) Liu, B.; Li, Y.; Cao, Y.; Wang, L.; Qing, S.; Wang, K.; Jia, D. Optimum Balance of Cu^{+} and Oxygen Vacancies of CuO_x-CeO_2 Composites for CO Oxidation Based on Thermal Treatment. *Eur. J. Inorg. Chem.* **2019**, *2019*, 1714−1723.
(16) Yu, W.-Z.; Wang, W.-W.; Li, S.-Q.; Fu, X.-P.; Wang, X.; Wu, K.; Si, R.; Ma, C.; Jia, C.-J.; Yan, C.-H. Construction of Active Site in a Sintered Copper-Ceria Nanorod Catalyst. *J. Am. Chem. Soc.* **2019**, *141*, 17548−17557.
(17) Alcala, R.; DeLaRiva, A.; Peterson, E. J.; Benavidez, A.; Garcia-Vargas, C. E.; Jiang, D.; Pereira-Hernández, X. I.; Brongersma, H. H.; Veen, R. ter.; Staněk, J.; Miller, J. T.; Wang, Y.; Datye, A. Atomically Dispersed Dopants for Stabilizing Ceria Surface Area. *Appl. Catal., B* **2021**, *284*, No. 119722.
(18) Rappé, K. G.; DiMaggio, C.; Pihl, J. A.; Theis, J. R.; Oh, S. H.; Fisher, G. B.; Parks, J.; Easterling, V. G.; Yang, M.; Stewart, M. L.; Howden, K. C. Aftertreatment Protocols for Catalyst Characterization and Performance Evaluation: Low-Temperature Oxidation, Storage, Three-Way, and NH_3-SCR Catalyst Test Protocols. *Emiss. Control Sci. Technol.* **2019**, *5*, 183−214.
(19) Pereira-Hernández, X. I.; DeLaRiva, A.; Muravev, V.; Kunwar, D.; Xiong, H.; Sudduth, B.; Engelhard, M.; Kovarik, L.; Hensen, E. J. M.; Wang, Y.; Datye, A. K. Tuning Pt-CeO_2 Interactions by High-Temperature Vapor-Phase Synthesis for Improved Reducibility of Lattice Oxygen. *Nat. Commun.* **2019**, *10*, No. 1358.
(20) Zhang, W. J.; Paldey, S.; Deevi, S. Effect of Moisture on the Active Species in Cu-CeO_2 Catalyst. *Appl. Catal., A* **2005**, *295*, 201−208.
(21) Lee, H. C.; Kim, D. H. Kinetics of CO and H_2 Oxidation over CuO-CeO_2 Catalyst in H_2 Mixtures with CO_2 and H_2O. *Catal. Today* **2008**, *132*, 109−116.
(22) Mullins, D. R. The Surface Chemistry of Cerium Oxide. *Surf. Sci. Rep.* **2015**, *70*, 42−85.
(23) Dong, L.; Yao, X.; Chen, Y.Interactions among Supported Copper-Based Catalyst Components and Their Effects on Performance: A Review. In *Cuihua Xuebao/Chinese Journal of Catalysis*; Science Press, May 1, 2013; pp 851−864. DOI: DOI: 10.1016/s1872-2067(12)60592-0.
(24) Yoshida, H.; Yamashita, N.; Ijichi, S.; Okabe, Y.; Misumi, S.; Hinokuma, S.; Machida, M. A Thermally Stable Cr−Cu Nanostructure Embedded in the CeO_2 Surface as a Substitute for Platinum-Group Metal Catalysts. *ACS Catal.* **2015**, *5*, 6738−6747.
(25) Nguyen, L.; Zhang, S.; Wang, L.; Li, Y.; Yoshida, H.; Patlolla, A.; Takeda, S.; Frenkel, A. I.; Tao, F. Reduction of Nitric Oxide with Hydrogen on Catalysts of Singly Dispersed Bimetallic Sites Pt_1Co_m and Pd_1Co_N. *ACS Catal.* **2016**, *6*, 840−850.
(26) Ning, J.; Zhou, Y.; Chen, A.; Li, Y.; Miao, S.; Shen, W. Dispersion of Copper on Ceria for the Low-Temperature Water-Gas Shift Reaction. *Catal. Today* **2020**, *357*, 460−467.
(27) Zabilskiy, M.; Djinović, P.; Tchernychova, E.; Tkachenko, O. P.; Kustov, L. M.; Pintar, A. Nanoshaped CuO/CeO_2 Materials: Effect of the Exposed Ceria Surfaces on Catalytic Activity in N_2O Decomposition Reaction. *ACS Catal.* **2015**, *5*, 5357−5365.
(28) Monte, M.; Gamarra, D.; López Cámara, A.; Rasmussen, S.; Gyorffy, N.; Schay, Z.; Martinez-Arias, A.; Conesa, J. Preferential Oxidation of CO in Excess H_2 over CuO/CeO_2 Catalysts: Performance as Function of the Copper Coverage and Exposed Face Present in the CeO_2 Support. *Catal. Today* **2014**, *229*, 104−113.
(29) Caputo, T.; Lisi, L.; Pirone, R.; Russo, G. On the Role of Redox Properties of CuO/CeO_2 Catalysts in the Preferential Oxidation of CO in H_2-Rich Gases. *Appl. Catal., A* **2008**, *348*, 42−53.
(30) Polychronopoulou, K.; Alkhoori, A. A.; Efstathiou, A. M.; Jaoude, M. A.; Damaskinos, C. M.; Baker, M. A.; Almutawa, A.; Anjum, D. H.; Vasiliades, M. A.; Belabbes, A.; Vega, L. F.; Zedan, A. F.; Hinder, S. J. Design Aspects of Doped CeO_2 for Low-Temperature Catalytic CO Oxidation: Transient Kinetics and DFT Approach. *ACS Appl. Mater. Interfaces* **2021**, *13*, 22391−22415.
(31) Payne, S. H.; Mcewen, J.-S.; Kreuzer, H. J.; Menzel, D. Adsorption and Desorption of CO on Ru(0001): A Comprehensive Analysis. *Surf. Sci.* **2005**, *594*, 240−262.
(32) Payne, S. H.; Mcewen, J.-S.; Kreuzer, H. J.; Menzel, D. Lateral Interactions and Nonequilibrium in Adsorption and Desorption. Part 2. A Kinetic Lattice Gas Model for (2×2)-(3O + NO)/Ru(001). *Surf. Sci.* **2006**, *600*, 4660−4669.
(33) Mcewen, J.-S.; Payne, S. H.; Kreuzer, H. J.; Kinne, M.; Denecke, R.; Steinrück, H.-P. Adsorption and Desorption of CO on Pt(111): A Comprehensive Analysis. *Surf. Sci.* **2003**, *545*, 47−69.
(34) Kim, Y.; Collinge, G.; Lee, M. S.; Khivantsev, K.; Cho, S. J.; Glezakou, V. A.; Rousseau, R.; Szanyi, J.; Kwak, J. H. Surface Density Dependent Catalytic Activity of Single Palladium Atoms Supported on Ceria**. *Angew. Chem., Int. Ed.* **2021**, *60*, 22769−22775.
(35) Nilius, N.; Kozlov, S. M.; Jerratsch, J. F.; Baron, M.; Shao, X.; Viñes, F.; Shaikhutdinov, S.; Neyman, K. M.; Freund, H. J. Formation of One-Dimensional Electronic States along the Step Edges of CeO_2(111). *ACS Nano* **2012**, *6*, 1126−1133.
(36) Lu, J. L.; Gao, H. J.; Shaikhutdinov, S.; Freund, H. J. Morphology and Defect Structure of the CeO_2(111) Films Grown on Ru(0001) as Studied by Scanning Tunneling Microscopy. *Surf. Sci.* **2006**, *600*, 5004−5010.
(37) Kunwar, D.; Zhou, S.; De La Riva, A.; Peterson, E.; Xiong, H.; Pereira Hernandez, X. I.; Purdy, S. C.; ter Veen, R.; Brongersma, H. H.; Miller, J. T.; Hashiguchi, H.; Kovarik, L.; Lin, S.; Guo, H.; Wang, Y.; Datye, A. Stabilizing High Metal Loadings of Thermally Stable Platinum Single Atoms on an Industrial Catalyst Support. *ACS Catal.* **2019**, *9*, 3978−3990.
(38) Dvořák, F.; Farnesi Camellone, M.; Tovt, A.; Tran, N.-D.; Negreiros, F. R.; Vorokhta, M.; Skála, T.; Matolínová, I.; Mysliveček, J.; Matolín, V.; Fabris, S. Creating Single-Atom Pt-Ceria Catalysts by Surface Step Decoration. *Nat. Commun.* **2016**, *7*, No. 10801.
(39) Bader, R. F. W.; Carroll, M. T.; Cheeseman, J. R.; Chang, C. Properties of Atoms in Molecules: Atomic Volumes. *J. Am. Chem. Soc.* **1987**, *109*, 7968−7979.
(40) Bader, R. F. W.; Nguyen-Dang, T. T. Quantum Theory of Atoms in Molecules−Dalton Revisited. *Adv. Quantum Chem.* **1981**, *14*, 63−124.
(41) Sanville, E.; Kenny, S. D.; Smith, R.; Henkelman, G. Improved Grid-Based Algorithm for Bader Charge Allocation. *J. Comput. Chem.* **2007**, *28*, 899−908.
(42) Henkelman, G.; Arnaldsson, A.; Jó Nsson, H.A Fast and Robust Algorithm for Bader Decomposition of Charge Density. DOI: 10.1016/j.commatsci.2005.04.010.
(43) Yu, M.; Trinkle, D. R. Accurate and Efficient Algorithm for Bader Charge Integration. *J. Chem. Phys.* **2011**, *134*, 064111.
(44) Wan, Q.; Wei, F.; Wang, Y.; Wang, F.; Zhou, L.; Lin, S.; Xie, D.; Guo, H. Single Atom Detachment from Cu Clusters, and Diffusion and Trapping on CeO2(111): Implications in Ostwald Ripening and Atomic Redispersion†. *Nanoscale* **2018**, *10*, 17893−17901.
(45) Wang, Y. G.; Mei, D.; Glezakou, V. A.; Li, J.; Rousseau, R. Dynamic Formation of Single-Atom Catalytic Active Sites on Ceria-Supported Gold Nanoparticles. *Nat. Commun* **2015**, *6*, No. 6511.
(46) Wang, Y. G.; Yoon, Y.; Glezakou, V. A.; Li, J.; Rousseau, R. The Role of Reducible Oxide-Metal Cluster Charge Transfer in Catalytic Processes: New Insights on the Catalytic Mechanism of CO Oxidation on Au/TiO_2 from Ab Initio Molecular Dynamics. *J. Am. Chem. Soc.* **2013**, *135*, 10673−10683.
(47) Jiang, D.; Wan, G.; García-Vargas, C. E.; Li, L.; Pereira-Hernández, X. I.; Wang, C.; Wang, Y. Elucidation of the Active Sites in Single-Atom Pd_1/CeO_2 Catalysts for Low-Temperature CO Oxidation. *ACS Catal.* **2020**, *10*, 11356−11364.
(48) Parkinson, G. S.; Novotny, Z.; Argentero, G.; Schmid, M.; Pavelec, J.; Kosak, R.; Blaha, P.; Diebold, U. Carbon Monoxide-Induced Adatom Sintering in a Pd−Fe_3O_4 Model Catalyst. *Nat. Mater.* **2013**, *12*, 724−728.
(49) Collinge, G.; Yuk, S. F.; Nguyen, M. T.; Lee, M. S.; Glezakou, V. A.; Rousseau, R.Effect of Collective Dynamics and Anharmonicity

on Entropy in Heterogenous Catalysis: Building the Case for Advanced Molecular Simulations. In *ACS Catalysis*; American Chemical Society, August 21, 2020; pp 9236−9260. DOI: DOI: 10.1021/acscatal.0c01501.
(50) Jones, J.; Xiong, H.; DeLaRiva, A. T.; Peterson, E. J.; Pham, H.; Challa, S. R.; Qi, G.; Oh, S.; Wiebenga, M. H.; Pereira Hernández, X. I.; Wang, Y.; Datye, A. K. Thermally Stable Single-Atom Platinum-on-Ceria Catalysts via Atom Trapping. *Science* **2016**, *353*, 150−154.
(51) Monti, D. A. M.; Baiker, A. Temperature-Programmed Reduction. Parametric Sensitivity and Estimation of Kinetic Parameters. *J. Catal.* **1983**, *83*, 323−335.
(52) Malet, P.; Caballero, A. The Selection of Experimental Conditions in Temperature-Programmed Reduction Experiments. *J. Chem. Soc., Faraday Trans. 1* **1988**, *84*, 2369−2375.
(53) Rieck, J. S.; Bell, A. T. Influence of Adsorption and Mass Transfer Effects on Temperature-Programmed Desorption from Porous Catalysts. *J. Catal.* **1984**, *85*, 143−153.
(54) Kreitz, B.; Wehinger, G. D.; Goldsmith, F.; Turek, T. Microkinetic Modeling of the CO_2 Desorption from Supported Multifaceted Ni Catalysts. *J. Phys. Chem. C* **2021**, *125*, 2984−3000.
(55) Rastegar, S. O.; Gu, T. Empirical Correlations for Axial Dispersion Coefficient and Peclet Number in Fixed-Bed Columns. *J. Chromatogr. A* **2017**, *1490*, 133−137.
(56) Ravel, B.; Newville, M.ATHENA, ARTEMIS, HEPHAESTUS: Data Analysis for X-Ray Absorption Spectroscopy Using IFEFFIT. In *Journal of Synchrotron Radiation*; International Union of Crystallography, 2005; Vol. *12*, pp 537−541. DOI: DOI: 10.1107/S0909049505012719.
(57) Nguyen, L.; Tao, F. F. Development of a Reaction Cell for *in-Situ/Operando* Studies of Surface of a Catalyst under a Reaction Condition and during Catalysis. *Rev. Sci. Instrum.* **2016**, *87*, No. 064101.
(58) Artiglia, L.; Orlando, F.; Roy, K.; Kopelent, R.; Safonova, O.; Nachtegaal, M.; Huthwelker, T.; van Bokhoven, J. A. Introducing Time Resolution to Detect Ce^{3+} Catalytically Active Sites at the Pt/CeO_2 Interface through Ambient Pressure X-Ray Photoelectron Spectroscopy. *J. Phys. Chem. Lett.* **2017**, *8*, 102−108.
(59) Skála, T.; Šutara, F.; Prince, K. C.; Matolín, V. Cerium Oxide Stoichiometry Alteration via Sn Deposition: Influence of Temperature. *J. Electron Spectrosc. Relat. Phenom.* **2009**, *169*, 20−25.
(60) Stadnichenko, A. I.; Muravev, V. V.; Koscheev, S. V.; Zaikovskii, V. I.; Aleksandrov, H. A.; Neyman, K. M.; Boronin, A. I. Study of Active Surface Centers of Pt/CeO_2 Catalysts Prepared Using Radio-Frequency Plasma Sputtering Technique. *Surf. Sci.* **2019**, *679*, 273−283.
(61) Kato, S.; Ammann, M.; Huthwelker, T.; Paun, C.; Lampimäki, M.; Lee, M.-T.; Rothensteiner, M.; van Bokhoven, J. A. Quantitative Depth Profiling of Ce^{3+} in Pt/CeO_2 by in Situ High-Energy XPS in a Hydrogen Atmosphere. *Phys. Chem. Chem. Phys.* **2015**, *17*, 5078−5083.
(62) Hutter, J.; Iannuzzi, M.; Schiffmann, F.; Vandevondele, J. Cp2k: Atomistic Simulations of Condensed Matter Systems. *Wiley Interdiscip. Rev.: Comput. Mol. Sci.* **2014**, *4*, 15−25.
(63) Goedecker, S.; Teter, M.; Hutter, J. Separable Dual-Space Gaussian Pseudopotentials. *Phys. Rev. B: Condens. Matter Mater. Phys.* **1996**, *54*, 1703−1710.
(64) Vandevondele, J.; Krack, M.; Mohamed, F.; Parrinello, M.; Chassaing, T.; Hutter, J. Quickstep: Fast and Accurate Density Functional Calculations Using a Mixed Gaussian and Plane Waves Approach. *Comput. Phys. Commun.* **2005**, *167*, 103−128.
(65) Lu, J. B.; Cantu, D. C.; Nguyen, M. T.; Li, J.; Glezakou, V. A.; Rousseau, R. Norm-Conserving Pseudopotentials and Basis Sets to Explore Lanthanide Chemistry in Complex Environments. *J. Chem. Theory Comput.* **2019**, *15*, 5987−5997.
(66) McQuarrie, D.*Statistical Mechanics*; Harper & Row: New York, 1975.
(67) Dudarev, S. L.; Botton, G.; et al. Electron-Energy-Loss Spectra and the Structural Stability of Nickel Oxide: An LSDA+U Study. *Phys. Rev. B: Condens. Matter Mater. Phys.* **1998**, *57*, 1505−1509.
(68) Campbell, C. T.; Sellers, J. R. V. The Entropies of Adsorbed Molecules. *J. Am. Chem. Soc.* **2012**, *134*, 18109−18115.
(69) Nosé, S. A Unified Formulation of the Constant Temperature Molecular Dynamics Methods. *J. Chem. Phys.* **1984**, *81*, 511−519.
(70) Hoover, W. G. Canonical Dynamics: Equilibrium Phase-Space Distributions. *Phys. Rev. A* **1985**, *31*, 1695−1697.
(71) Allen, M. P.; Tildesley, D. J.*Computer Simulation of Liquids*; Oxford University Press, 2017; pp 1−626 DOI: 10.1093/oso/9780198803195.001.0001.